

Constraints on dark matter models from a *Fermi* LAT search for high-energy cosmic-ray electrons from the Sun

M. Ajello,¹ W. B. Atwood,² L. Baldini,³ G. Barbiellini,^{4,5} D. Bastieri,^{6,7} R. Bellazzini,³ B. Berenji,¹ R. D. Blandford,¹ E. D. Bloom,¹ E. Bonamente,^{8,9} A. W. Borgland,¹ E. Bottacini,¹ A. Bouvier,² J. Bregeon,³ M. Brigida,^{10,11} P. Bruel,¹² R. Buehler,¹ S. Buson,^{6,7} G. A. Caliendo,¹³ R. A. Cameron,¹ P. A. Caraveo,¹⁴ C. Cecchi,^{8,9} E. Charles,¹ A. Chekhtman,¹⁵ S. Ciprini,^{16,9} R. Claus,¹ J. Cohen-Tanugi,¹⁷ S. Cutini,¹⁸ A. de Angelis,¹⁹ F. de Palma,^{10,11} C. D. Dermer,²⁰ S. W. Digel,¹ E. do Couto e Silva,¹ P. S. Drell,¹ C. Favuzzi,^{10,11} S. J. Fegan,¹² W. B. Focke,¹ Y. Fukazawa,²¹ P. Fusco,^{10,11} F. Gargano,¹¹ N. Gehrels,²² S. Germani,^{8,9} N. Giglietto,^{10,11} F. Giordano,^{10,11} M. Giroletti,²³ T. Glanzman,¹ G. Godfrey,¹ I. A. Grenier,²⁴ S. Guiriec,²⁵ M. Gustafsson,⁶ D. Hadasch,¹³ G. Iafrate,^{4,26} G. Jóhannesson,²⁷ A. S. Johnson,¹ T. Kamae,¹ H. Katagiri,²⁸ J. Kataoka,²⁹ M. Kuss,³ L. Latronico,³ A. M. Lionetto,^{30,31} F. Longo,^{4,5} F. Loparco,^{10,11,*} M. N. Lovellette,²⁰ P. Lubrano,^{8,9} M. N. Mazziotta,^{11,†} J. E. McEnery,^{22,32} P. F. Michelson,¹ T. Mizuno,²¹ C. Monte,^{10,11} M. E. Monzani,¹ A. Morselli,³⁰ I. V. Moskalenko,¹ S. Murgia,¹ M. Naumann-Godo,²⁴ J. P. Norris,³³ E. Nuss,¹⁷ T. Ohsugi,³⁴ N. Omodei,¹ E. Orlando,^{1,35} J. F. Ormes,³⁶ M. Ozaki,³⁷ D. Paneque,^{38,1} J. H. Panetta,¹ M. Pesce-Rollins,³ M. Pierbattista,²⁴ F. Piron,¹⁷ S. Rainò,^{10,11} R. Rando,^{6,7} M. Razzano,³ A. Reimer,^{39,1} O. Reimer,^{39,1} S. Ritz,² T. L. Schalk,² C. Sgrò,³ J. Siegal-Gaskins,^{40,‡} E. J. Siskind,⁴¹ P. D. Smith,⁴⁰ G. Spandre,³ P. Spinelli,^{10,11} D. J. Suson,⁴² H. Takahashi,³⁴ T. Tanaka,¹ J. G. Thayer,¹ J. B. Thayer,¹ L. Tibaldo,^{6,7,24,43} G. Tosti,^{8,9} E. Troja,^{22,44} T. L. Usher,¹ J. Vandenbroucke,¹ V. Vasileiou,¹⁷ G. Vianello,^{1,45} N. Vilchez,^{46,47} A. P. Waite,¹ P. Wang,¹ B. L. Winer,⁴⁰ K. S. Wood,²⁰ Z. Yang,^{48,49} and S. Zimmer^{48,49}

¹W. W. Hansen Experimental Physics Laboratory,
Kavli Institute for Particle Astrophysics and Cosmology,
Department of Physics and SLAC National Accelerator Laboratory,
Stanford University, Stanford, CA 94305, USA

²*Santa Cruz Institute for Particle Physics,*
Department of Physics and Department of Astronomy and Astrophysics,
University of California at Santa Cruz,
Santa Cruz, CA 95064, USA

³*Istituto Nazionale di Fisica Nucleare,*
Sezione di Pisa, I-56127 Pisa, Italy

⁴*Istituto Nazionale di Fisica Nucleare,*
Sezione di Trieste, I-34127 Trieste, Italy

⁵*Dipartimento di Fisica,*
Università di Trieste, I-34127 Trieste, Italy

⁶*Istituto Nazionale di Fisica Nucleare,*
Sezione di Padova, I-35131 Padova, Italy

⁷*Dipartimento di Fisica “G. Galilei”,*
Università di Padova, I-35131 Padova, Italy

⁸*Istituto Nazionale di Fisica Nucleare,*
Sezione di Perugia, I-06123 Perugia, Italy

⁹*Dipartimento di Fisica, Università degli Studi di Perugia,*
I-06123 Perugia, Italy

¹⁰*Dipartimento di Fisica “M. Merlin” dell’Università e del Politecnico di Bari,*
I-70126 Bari, Italy

¹¹*Istituto Nazionale di Fisica Nucleare,*
Sezione di Bari, 70126 Bari, Italy

¹²*Laboratoire Leprince-Ringuet, École polytechnique,*
CNRS/IN2P3, Palaiseau, France

¹³*Institut de Ciències de l’Espai (IEEE-CSIC),*
Campus UAB, 08193 Barcelona, Spain

¹⁴*INAF-Istituto di Astrofisica Spaziale e Fisica Cosmica,*
I-20133 Milano, Italy

¹⁵*Artep Inc., 2922 Excelsior Springs Court, Ellicott City,*
MD 21042, resident at Naval Research Laboratory,
Washington, DC 20375, USA

¹⁶*ASI Science Data Center, I-00044 Frascati (Roma), Italy*

¹⁷*Laboratoire Univers et Particules de Montpellier,*
Université Montpellier 2,
CNRS/IN2P3, Montpellier, France

- ¹⁸*Agenzia Spaziale Italiana (ASI) Science Data Center,
I-00044 Frascati (Roma), Italy*
- ¹⁹*Dipartimento di Fisica,
Università di Udine and Istituto Nazionale di Fisica Nucleare,
Sezione di Trieste, Gruppo Collegato di Udine,
I-33100 Udine, Italy*
- ²⁰*Space Science Division, Naval Research Laboratory,
Washington, DC 20375-5352, USA*
- ²¹*Department of Physical Sciences, Hiroshima University,
Higashi-Hiroshima, Hiroshima 739-8526, Japan*
- ²²*NASA Goddard Space Flight Center,
Greenbelt, MD 20771, USA*
- ²³*INAF Istituto di Radioastronomia, 40129 Bologna, Italy*
- ²⁴*Laboratoire AIM, CEA-IRFU/CNRS/Université Paris Diderot,
Service d'Astrophysique, CEA Saclay,
91191 Gif sur Yvette, France*
- ²⁵*Center for Space Plasma and Aeronomic Research (CSPAR),
University of Alabama in Huntsville,
Huntsville, AL 35899, USA*
- ²⁶*Osservatorio Astronomico di Trieste,
Istituto Nazionale di Astrofisica, I-34143 Trieste, Italy*
- ²⁷*Science Institute, University of Iceland,
IS-107 Reykjavik, Iceland*
- ²⁸*College of Science, Ibaraki University,
2-1-1, Bunkyo, Mito 310-8512, Japan*
- ²⁹*Research Institute for Science and Engineering,
Waseda University, 3-4-1, Okubo,
Shinjuku, Tokyo 169-8555, Japan*
- ³⁰*Istituto Nazionale di Fisica Nucleare,
Sezione di Roma "Tor Vergata", I-00133 Roma, Italy*
- ³¹*Dipartimento di Fisica,
Università di Roma "Tor Vergata", I-00133 Roma, Italy*
- ³²*Department of Physics and Department of Astronomy,
University of Maryland, College Park, MD 20742, USA*
- ³³*Department of Physics, Boise State University,
Boise, ID 83725, USA*
- ³⁴*Hiroshima Astrophysical Science Center,
Hiroshima University, Higashi-Hiroshima,
Hiroshima 739-8526, Japan*
- ³⁵*Max-Planck Institut für extraterrestrische Physik,
85748 Garching, Germany*
- ³⁶*Department of Physics and Astronomy,
University of Denver, Denver, CO 80208, USA*
- ³⁷*Institute of Space and Astronautical Science,
JAXA, 3-1-1 Yoshinodai, Chuo-ku,
Sagamihara, Kanagawa 252-5210, Japan*
- ³⁸*Max-Planck-Institut für Physik,
D-80805 München, Germany*
- ³⁹*Institut für Astro- und Teilchenphysik and Institut für Theoretische Physik,
Leopold-Franzens-Universität Innsbruck,
A-6020 Innsbruck, Austria*
- ⁴⁰*Department of Physics,
Center for Cosmology and Astro-Particle Physics,
The Ohio State University, Columbus, OH 43210, USA*
- ⁴¹*NYCB Real-Time Computing Inc.,
Lattingtown, NY 11560-1025, USA*
- ⁴²*Department of Chemistry and Physics,
Purdue University Calumet,
Hammond, IN 46323-2094, USA*
- ⁴³*Partially supported by the International Doctorate on Astroparticle Physics (IDAPP) program*
- ⁴⁴*NASA Postdoctoral Program Fellow, USA*
- ⁴⁵*Consorzio Interuniversitario per la Fisica Spaziale (CIFS),
I-10133 Torino, Italy*
- ⁴⁶*CNRS, IRAP, F-31028 Toulouse cedex 4, France*

⁴⁷*Université de Toulouse, UPS-OMP, IRAP, Toulouse, France*

⁴⁸*Department of Physics, Stockholm University,
AlbaNova, SE-106 91 Stockholm, Sweden*

⁴⁹*The Oskar Klein Centre for Cosmoparticle Physics,
AlbaNova, SE-106 91 Stockholm, Sweden*

(Dated: July 22, 2011)

During its first year of data taking, the Large Area Telescope (LAT) onboard the *Fermi* Gamma-Ray Space Telescope has collected a large sample of high-energy cosmic-ray electrons and positrons (CREs). We present the results of a directional analysis of the CRE events, in which we searched for a flux excess correlated with the direction of the Sun. Two different and complementary analysis approaches were implemented, and neither yielded evidence of a significant CRE flux excess from the Sun. We derive upper limits on the CRE flux from the Sun's direction, and use these bounds to constrain two classes of dark matter models which predict a solar CRE flux: (1) models in which dark matter annihilates to CREs via a light intermediate state, and (2) inelastic dark matter models in which dark matter annihilates to CREs.

PACS numbers: 96.50.S-, 95.35.+d

Keywords: Cosmic Rays, Electrons, Fermi, Sun

I. INTRODUCTION

In the last decades the searches for a dark matter (DM) signal from the Sun were performed looking for possible excesses of neutrinos or gamma-rays associated with the Sun's direction. However, as it was noted in Ref. [1], several DM models that have been recently developed to explain various experimental results also imply an associated solar flux of high-energy cosmic-ray electrons and positrons (CREs). On the other hand, no known astrophysical mechanisms are expected to generate a significant high-energy CRE (> 100 GeV) excess associated with the Sun.

A class of models in which DM annihilates to CREs through a new light intermediate state ϕ [2, 3] has been considered to explain the excesses in local CRE fluxes reported by PAMELA [4], ATIC [5], and *Fermi* [6, 7]. In these scenarios DM particles captured by the Sun through elastic scattering interactions would annihilate to ϕ pairs in the Sun's core, and if the ϕ could escape the surface of the Sun before decaying to CREs, these models could produce an observable CRE flux.

Another class of models in which DM scatters off of nucleons predominantly via inelastic scattering has been proposed as a means of reconciling the results of DAMA and DAMA/LIBRA [8, 9] with CDMS-II [10, 11] and other experiments (e.g., [12, 13]; see also [14] for a comprehensive discussion of experimental constraints). If DM is captured by the Sun only through inelastic scattering (iDM), this could lead to a non-negligible fraction of DM annihilating outside of the Sun's surface. For models in which iDM annihilates to CREs, an observable flux at energies above a few tens of GeV could be produced.

During its first year of operation, the Large Area Telescope (LAT) onboard the *Fermi* satellite [15] has collected a substantial number of CRE events, which has allowed a precise measurement of the energy spectrum over a broad energy range from a few GeV up to 1 TeV [6, 7]. Furthermore, a directional analysis of the high-energy CRE events was performed in the Galactic reference frame [16], and showed no evidence of anisotropies.

In this paper we use the high-energy CRE data set to search for flux variations correlated with the Sun's direction. Since the Sun is moving with respect to the Galactic reference frame, the previously-reported absence of anisotropies in the CRE flux observed in the Galactic frame does not necessarily imply a negative result.

II. DATA SELECTION

The *Fermi* LAT is a pair-conversion telescope designed to detect gamma rays in the energy range from 20 MeV to more than 300 GeV. A full description of the apparatus is given in [15]. Even though it is a photon detector, it has been demonstrated that the LAT is also an excellent CRE detector [6, 7, 16]. For this analysis we used the CRE data sample collected by the LAT during its first year of operation, starting from August 4, 2008. The event selection was performed in the same way as in Ref. [16]; approximately 1.35×10^6 CRE events with energies larger than 60 GeV passed the selection cuts. As discussed in Ref. [16], the energy threshold of 60 GeV was chosen because it is higher than the geomagnetic cutoff in any part of *Fermi*'s orbit.

Unlike gamma rays, CREs are deflected by interactions with magnetic fields encountered during their propagation in interstellar space. In particular, CREs coming from the Sun are deflected by both the Sun's and the Earth's magnetic fields.

Geomagnetic effects on CREs have been studied using a code that reconstructs the trajectories of charged particles in the Earth's magnetic field based on the Interna-

*Electronic address: loparco@ba.infn.it

†Electronic address: mazziotta@ba.infn.it

‡Electronic address: jsg@mps.ohio-state.edu

tional Geomagnetic Reference Field (IGRF) model [17]. Since the *Fermi* LAT cannot measure the sign of the electric charge, we associated both an electron and a positron track with each CRE event detected by the LAT. Each track starts from the detection point with the same energy of the event and with a direction opposite to that of the event, and ends at a very large distance (larger than 100 Earth-radii from the Earth's center).

The distribution of deflection angles at different energies was analyzed. The simulation demonstrated that, at energies above 20 GeV, 90% of the particles are deflected with respect to the original direction within an angle $\delta_{90\%}$ given by the approximate formula:

$$\delta_{90\%} \approx \frac{2.8^\circ}{E(\text{TeV})} \quad (1)$$

where E is the particle energy. Hence, due to the geomagnetic field, the reconstructed directions of CREs with energies above 100 GeV detected by the LAT and coming from any given direction of the sky will be spread over a cone with an angular radius of about 30° centered on the original incoming direction.

The directions of incoming CREs are also affected by the Heliospheric Magnetic Field. A detailed study of its effects on CREs is beyond the scope of this work, however in Ref. [18], it was shown that CREs with energies of several hundreds of GeV can travel through the center of the solar system without experiencing significant deflections.

CREs travelling in the Solar System may also suffer energy losses, mainly due to the Inverse Compton (IC) scatterings on the photons emitted by the Sun and to the synchrotron radiation (SR) emitted in the interactions with the Heliospheric Magnetic Field. To study the energy loss processes of CREs travelling from the Sun to the Earth we implemented a simple toy model, in which we assumed that CREs propagate from the Sun's surface to the Earth in straight lines and with velocity c . Following Ref. [19], we assumed that the Sun can be modeled as a black body with a temperature of 5777 K and with a photon density given by:

$$N_{ph}(\epsilon, r) = 0.5n_{bb}(\epsilon) \left[1 - \sqrt{1 - \frac{R_\odot^2}{r^2}} \right] \quad (2)$$

where $n_{bb}(\epsilon)$ is the blackbody photon energy density (Planck's equation), R_\odot is the solar radius and r is the distance from the center of the Sun. The IC energy loss rate of CREs was then evaluated as in Ref. [20] as:

$$-\left(\frac{dE}{dt}\right)_{IC} = \frac{4}{3}\sigma_T c W \beta^2 \frac{\gamma_k^2 \gamma^2}{\gamma_k^2 + \gamma^2} \quad (3)$$

where βc and γ are respectively the velocity and the Lorentz factor of the CRE, W is the photon energy

density evaluated from eq. 2, σ_T is the Thomson cross section and γ_k is given by:

$$\gamma_k = \frac{3\sqrt{5}m_e c^2}{8\pi k_B T} \quad (4)$$

where m_e is the electron mass, k_B is the Boltzmann's constant and $T = 5777\text{K}$ is the temperature of the Sun's surface. The evaluation of the SR energy loss rate is not easy, because the structure of the Heliospheric Magnetic Field is rather complex [21]. However, as a first approximation, we assumed that the strength of the Heliospheric Magnetic Field drops from the Sun's surface as:

$$B(r) = B_0 \frac{R_\odot^2}{r^2} \quad (5)$$

where $B_0 = 1\text{ gauss}$ is the strength of the field on the Sun's surface. We did not include the contribution of the Geomagnetic field to synchrotron energy losses because, even though the field strength at the LAT altitude is of the order of 1 gauss, the path length of CREs in the Geomagnetic field is of the order of a few Earth radii, which is negligible with respect to the path length in the Heliospheric Magnetic field, which is of the order of a few solar radii.

The synchrotron energy loss rate of CREs was then calculated as [22]:

$$-\left(\frac{dE}{dt}\right)_S = \frac{4}{3}\sigma_T c W_B \beta^2 \gamma^2 \quad (6)$$

where W_B is the magnetic field energy density that includes only the contribution from the Heliospheric Magnetic Field and, in our model, results to be negligible with respect to the IC energy loss rate. Using eqs. 3 and 6, we calculated that CREs in the energy range from 60 GeV to 1 TeV travelling from the Sun to the Earth lose no more than 2% of their initial energy. Therefore, in the calculations of the following sections, we will neglect all energy loss processes.

III. DATA ANALYSIS AND RESULTS

To study the CRE flux from the Sun's direction and to search for variations with respect to the average flux, we implemented two complementary analysis approaches: (i) flux asymmetry analysis and (ii) comparison of the solar flux with the isotropic flux.

A. Flux asymmetry studies

This approach compares the CRE flux from the Sun with the flux from a fake source (fake Sun) placed in the

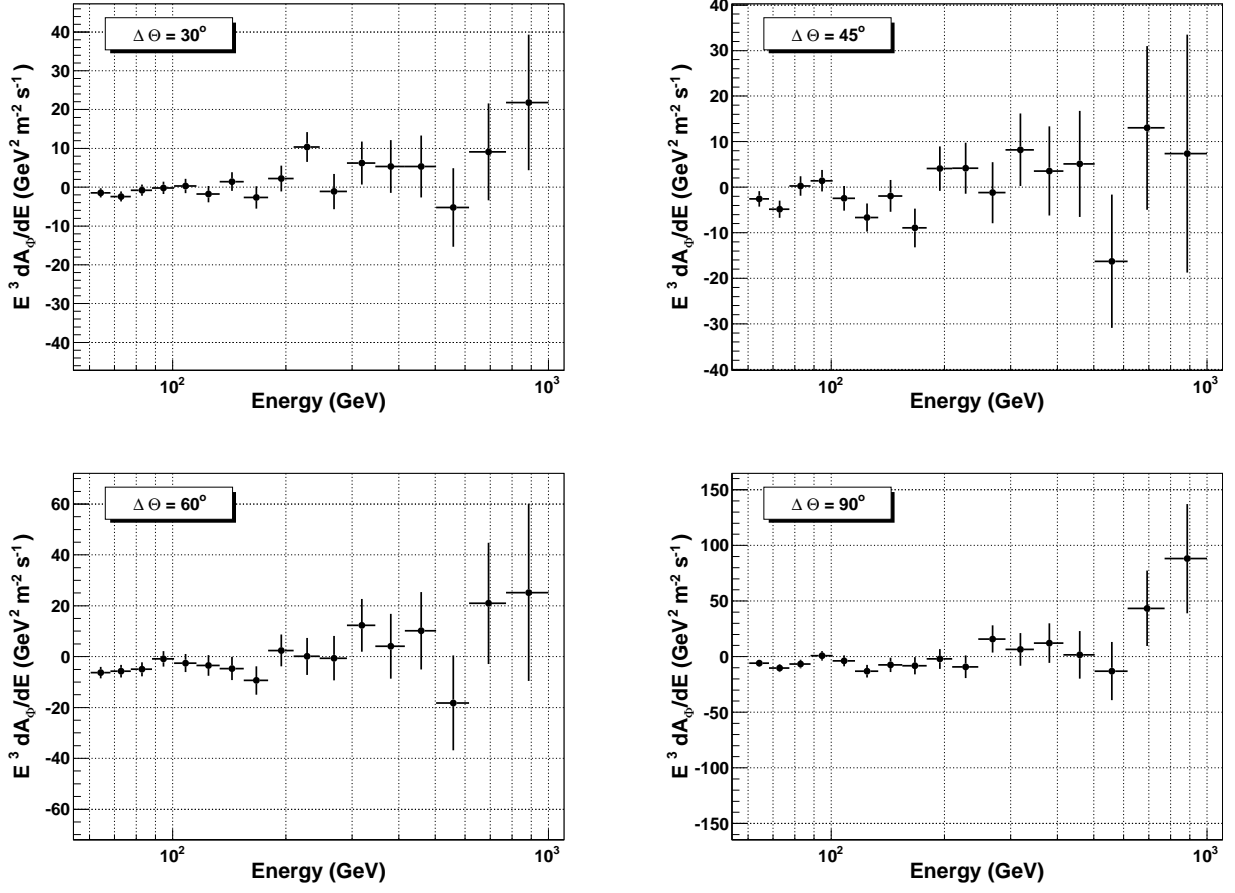


FIG. 1: Differential flux asymmetry between real and fake Sun evaluated in cones with angular radii $\Delta\Theta = 30^\circ$ (top left panel), 45° (top right panel), 60° (bottom left panel) and 90° (bottom right panel). The fluxes are multiplied by E^3 (the energy values correspond to the bin centers) since the energy spectrum of CREs is approximately proportional to E^{-3} in this energy range. Only statistical error bars are shown.

Angular radius	Maximum deviation (σ_{max})	$P(\sigma_{max})$	$P(\sigma > \sigma_{max})$
30°	2.690	0.007	0.113
45°	-2.542	0.011	0.171
60°	-2.806	0.005	0.082
90°	-2.947	0.003	0.050

TABLE I: For each cone used for the flux asymmetry analysis the maximum deviations (either positive or negative) from the null value are shown and the corresponding probabilities of observing larger values in the hypothesis of null flux asymmetry. The last column shows the probability of finding at least one energy bin with a larger flux asymmetry than the maximum observed value.

sky position opposite to that of the Sun. To perform our analyses, we chose a custom reference frame derived from ecliptic coordinates. The ecliptic coordinates associated with each CRE event were evaluated from equatorial coordinates using the formulae in Ref. [23]. Indicating with (λ, β) the pair of ecliptic coordinates (longitude and latitude, respectively) associated with any given direction, the Sun's direction will always lie in the plane $\beta = 0$. In fact, since the Sun is moving eastwards along the path of the ecliptic, its ecliptic latitude will always

be zero by definition, while its ecliptic longitude will always increase, describing a complete 360° cycle in one year [23]. In our custom reference frame, the coordinates associated with each direction are defined as:

$$\begin{cases} \lambda' = \lambda - \lambda_{Sun} \\ \beta' = \beta \end{cases} \quad (7)$$

where λ_{Sun} is the ecliptic longitude of the Sun, evaluated from the Sun's ephemeris using a software interfaced to the JPL libraries [24]. In this reference frame, the Sun's coordinates will always be ($\lambda'_{Sun} = 0^\circ, \beta'_{Sun} = 0^\circ$). On the other hand, the fake Sun will always be located at the coordinates ($\lambda'_{fake\ Sun} = 180^\circ, \beta'_{fake\ Sun} = 0^\circ$).

Due to the geomagnetic field's effects on CRE trajectories described in §II, we consider the fluxes from extended sky regions centered on the Sun (and on the fake Sun). In particular, we compare the CRE fluxes from directions within cones of angular radii $\Delta\Theta$, centered on the position of the Sun and the fake Sun. According to Eq. 1, 90% of CREs with energies of 100 GeV are deflected within a cone of about 30° angular radius, and so we chose this value as the minimum angular radius of the sky regions to be investigated because the DM models discussed in Ref. [1] predict a CRE flux excess from the Sun in the energy range above 100 GeV.

To measure the fluxes from different sky regions, we first divided the sky into a grid of pixels, then evaluated the CRE fluxes from individual pixels (each pixel was treated as a point source), and finally integrated the fluxes from the pixels belonging to the selected sky regions. We used the HEALPix [25] pixelization scheme, and divided the sky into 12288 equal-area pixels, each covering a solid angle of about 10^{-3} sr. The CRE differential fluxes from individual pixels were evaluated according to the following equation:

$$\frac{d\Phi_i(E)}{dE} = \frac{1}{\Delta E} \frac{N_i(E) \times (1 - c(E))}{\mathcal{E}_i(E)} \quad (8)$$

where $d\Phi_i(E)/dE$ is the differential CRE flux (expressed in particles per unit energy, unit area and unit time) in the energy interval $[E, E + \Delta E]$ from the i th pixel, $N_i(E)$ is the number of observed CRE events from the i th pixel with energies between E and $E + \Delta E$, $c(E)$ is the residual contamination (the contamination values are reported in Ref. [7]) and $\mathcal{E}_i(E)$ is the exposure of the i th pixel, which is calculated taking into account the effective area of the instrument, and the live time of the i th pixel. The dependence of the effective area on the CRE direction in the instrument, expressed in terms of the off-axis and azimuth angles θ and ϕ , is also taken into account in the calculation.

The CRE flux from a cone of angular radius $\Delta\Theta$ centered on the Sun is then given by:

$$\frac{d\Phi_{Sun}(E|\Delta\Theta)}{dE} = \sum_{i \in ROI(\Delta\Theta)} \frac{d\Phi_i(E)}{dE} \quad (9)$$

where $ROI(\Delta\Theta)$ denotes the set of pixels (region of interest) at an angular distance less than $\Delta\Theta$ from the Sun. The flux from the fake Sun is evaluated in a similar way. The flux asymmetry can then be evaluated as:

$$\frac{dA_\Phi(E|\Delta\Theta)}{dE} = \frac{d\Phi_{Sun}(E|\Delta\Theta)}{dE} - \frac{d\Phi_{Fake\ Sun}(E|\Delta\Theta)}{dE} \quad (10)$$

The variable $dA_\Phi(E|\Delta\Theta)/dE$ defined in Eq. 10 is the difference between the CRE flux from the Sun and the fake Sun; the flux of the fake Sun is assumed to be representative of the average CRE flux across the sky. Positive (negative) values of $dA_\Phi(E|\Delta\Theta)/dE$ indicate an excess (deficit) of CREs from the Sun. We emphasize that this approach relies on the assumption that the flux from the fake Sun region is representative of the average CRE flux.

In Fig. 1 the differential CRE flux asymmetries $dA_\Phi(E|\Delta\Theta)/dE$ between the real and the fake Sun are shown for four different ROIs, with angular radii of 30° , 45° , 60° and 90° . No significant CRE flux excesses or deficits from the Sun are observed at any energy. In the plots of Fig. 1 only statistical error bars are shown. As pointed out in Ref. [7], the main source of systematic uncertainties in the evaluation of CRE fluxes is the imperfect knowledge of the detector's effective area. Assuming that it is affected only by a normalization error, when calculating the error on the flux differences $dA_\Phi(E|\Delta\Theta)/dE$, the contribution from the normalization error will be proportional to $|dA_\Phi(E|\Delta\Theta)/dE|$ (see the discussion in Ref. [26]), and therefore it will be negligible with respect to the statistical error.

Assuming that the measured flux asymmetries in each energy bin behave as Gaussian random variables, we expressed the excesses and deficits (with respect to the hypothesis of a null flux asymmetry) in units of σ (σ is the statistical error associated with each measurement), and evaluated the corresponding probabilities of measuring larger excesses or deficits assuming the null hypothesis. Table I shows, for each value of the angular radius $\Delta\Theta$, the maximum observed deviations from the null flux asymmetry in units of σ , and the corresponding probabilities of measuring larger flux asymmetries in the null hypothesis. As shown in Table I, the flux asymmetries in all of the ROIs are always within 3σ of zero. The last column of Table I shows the probabilities of finding, in each ROI, at least one energy bin with a flux asymmetry larger than the maximum observed value. The probabilities were calculated assuming that the flux asymmetries measured in each of the 17 energy bins used in our analysis are uncorrelated. The calculations were performed taking only statistical errors into account; if systematic errors were also taken into account, the significance of the deviations of the flux asymmetries from zero would be smaller.

The same analysis was repeated for integral fluxes above various energy thresholds and again no evidence of flux asymmetries was found.

1. Evaluation of statistical upper limits on the CRE flux asymmetry

The previous analysis did not provide any evidence of a CRE flux excess from the Sun with respect to the fake Sun, so we set statistical upper limits on this signal by following the approach outlined in Ref. [27] (pp. 136-139). In each energy bin, the measured flux asymmetry $dA_\Phi(E|\Delta\Theta)/dE$ can be seen as a realization of a Gaussian random variable. Assuming the hypothesis of a CRE flux excess from the Sun, its expectation value must be non-negative:

$$\left\langle \frac{dA_\Phi(E|\Delta\Theta)}{dE} \right\rangle \geq 0 \quad (11)$$

To set upper limits on $\langle dA_\Phi(E|\Delta\Theta)/dE \rangle$ we implemented the Bayesian method described in Ref. [27], assuming a uniform prior density. The σ of the Gaussian probability distribution function associated with each measurement of $dA_\Phi(E|\Delta\Theta)/dE$ is the statistical error associated with the measurement.

Fig. 2 shows the statistical upper limits on CRE flux asymmetries at different confidence levels, considering different cones centered on the Sun with angular radii ranging from 30° to 90° . In Table II the values of the upper limits at 95% confidence level for the flux asymmetry $dA_\Phi(E|\Delta\Theta)/dE$ in the different ROIs are summarized. The calculated upper limits are also expressed in terms of fractions of the CRE flux from the region of the fake Sun.

B. Comparison with an isotropic flux

The second approach used in this analysis is based on the event-shuffling technique employed in Ref. [16], which was used to build a simulated sample of isotropic CREs starting from the real events. Simulated events are built by randomly coupling the arrival times and the arrival directions (in local instrument coordinates) of real events. The simulated event sample used for this analysis is the same used in Ref. [16] and is 100 times larger than the real one.

In this case, given the angular radius $\Delta\Theta$ of a cone centered on the Sun, we evaluated the count differences between real and simulated CREs as:

$$\Delta N(E|\Delta\Theta) = N_{real}(E|\Delta\Theta) - \alpha(E)N_{sim}(E|\Delta\Theta) \quad (12)$$

where $N_{real}(E|\Delta\Theta)$ and $N_{sim}(E|\Delta\Theta)$ are respectively the number of CRE events in the real and simulated data sets with energy E and arrival directions within the selected cone. The parameter $\alpha(E)$ in Eq. 12 is a normalization factor. If $N_{real}(E)$ and $N_{sim}(E)$ are the total numbers of real and simulated events with energy E , then $\alpha(E) = N_{real}(E)/N_{sim}(E)$ [48].

The count difference is finally converted into a flux asymmetry according to the following equation:

$$\frac{dA'_\Phi(E|\Delta\Theta)}{dE} = \frac{1}{\Delta E} \cdot \frac{\Delta N(E|\Delta\Theta)(1 - c(E))}{\mathcal{E}(E|\Delta\Theta)} \quad (13)$$

where $c(E)$ is the residual contamination and $\mathcal{E}(E|\Delta\Theta)$ is the exposure of the selected sky region, which is evaluated from the instrument effective area and the live times of the pixels belonging to that sky region.

We emphasize that the two approaches used in this work are complementary, but not fully equivalent. In the first case the variable $dA_\Phi(E|\Delta\Theta)/dE$ is built using real events from different directions (real Sun and fake Sun). On the other hand, in the second case, the variable $dA'_\Phi(E|\Delta\Theta)/dE$ is built using real and simulated events from the same region of the sky. In both cases the goal of the analysis is to compare the CRE flux from the Sun with the average CRE flux. In the first case, the reference flux is evaluated looking at real events from the fake Sun region, while in the second case it is evaluated simulating an isotropic flux and looking at simulated events from the Sun region.

The second approach, however, excludes potential systematic biases when calculating flux differences. In particular, to evaluate the flux from a given region of the sky requires knowledge of the exposure, which in turn depends on the effective area of the detector and on the observation live time. The effective area is calculated from Monte Carlo simulations and thus could be affected by systematics such as variations correlated with time and spacecraft position or miscalculations of its dependence on instrument coordinates. When evaluating the flux asymmetry $dA_\Phi(E|\Delta\Theta)/dE$ according to Eq. 10, the systematic uncertainties involved in the evaluation of the two terms could be different, and the result could be biased. On the other hand, when evaluating the flux difference $dA'_\Phi(E|\Delta\Theta)/dE$ from Eq. 13, inaccuracies in the effective area calculation can only result in a scale error on the flux difference.

To determine whether the real counts differ significantly from the simulated ones, we performed a hypothesis test following the prescriptions of Ref. [28]. Denoting with $N_{real}(E|\Delta\Theta)$ and $N_{sim}(E|\Delta\Theta)$ the real and the simulated counts in the energy bin E , the null hypothesis for this analysis is that $N_{real}(E|\Delta\Theta) = \alpha(E)N_{sim}(E|\Delta\Theta)$. Following Ref. [28], we evaluated the significance in each energy bin as:

$$S(E|\Delta\Theta) = \pm\sqrt{2} \left\{ N_{real}(E|\Delta\Theta) \ln \left[\frac{1 + \alpha(E)}{\alpha(E)} \right] \frac{N_{real}(E|\Delta\Theta)}{N_{real}(E|\Delta\Theta) + N_{sim}(E|\Delta\Theta)} + N_{sim}(E|\Delta\Theta) \ln \left[(1 + \alpha(E)) \frac{N_{sim}(E|\Delta\Theta)}{N_{real}(E|\Delta\Theta) + N_{sim}(E|\Delta\Theta)} \right] \right\}^{1/2} \quad (14)$$

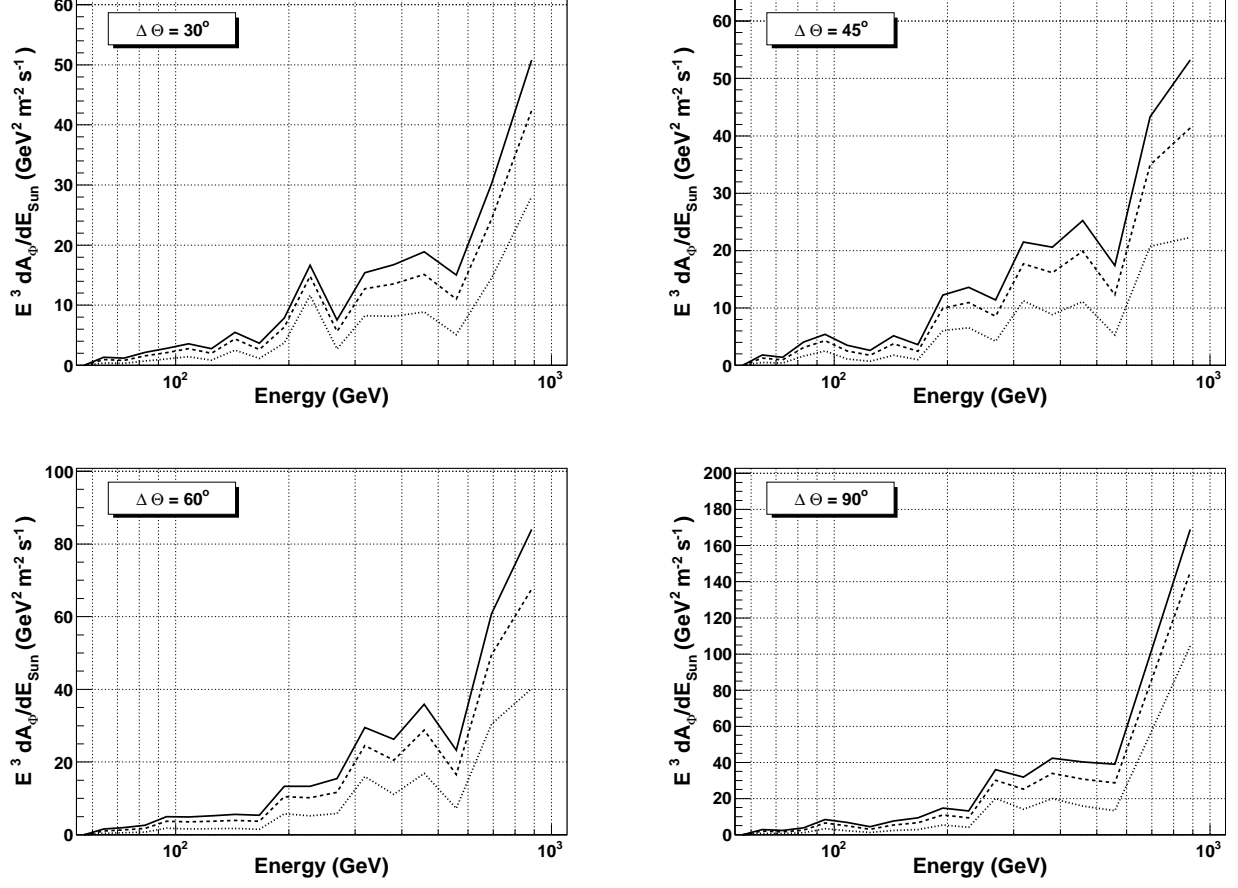


FIG. 2: Statistical upper limits at confidence levels of 68% (dotted lines), 95% (dashed lines) and 99% (continuous lines) for the CRE flux asymmetry between real and fake Sun, evaluated in cones with angular radii $\Delta\Theta = 30^\circ$ (top left panel), 45° (top right panel), 60° (bottom left panel) and 90° (bottom right panel).

with the convention of choosing the $+$ sign if $N_{real}(E|\Delta\Theta) > \alpha(E)N_{sim}(E|\Delta\Theta)$ and the $-$ sign if $N_{real}(E|\Delta\Theta) < \alpha(E)N_{sim}(E|\Delta\Theta)$.

The significance values evaluated from Eq. 14 can be converted into probability values. In particular, since S^2 is a random variable following a χ^2 distribution with 1 degree of freedom [28], one can easily evaluate the probability of observing a value of S^2 larger than the one observed. In Table III the maximum deviations from the null flux asymmetries are shown for each ROI used for our analysis, together with the corresponding probabilities of finding larger deviations. The last column of the table shows the probabilities of finding, in each ROI, at least one energy bin with a flux asymmetry larger than the maximum observed value. Again, these probabilities were calculated assuming that the flux asymmetries measured in each of the 17 energy bins used for our analysis are uncorrelated. The observed deviations from the null flux asymmetries are statistically insignificant.

The count differences were converted into flux differences according to Eq. 13. In Fig. 3 the asymmetry variable $dA'_\Phi(E|\Delta\Theta)/dE$ between the real and simulated

fluxes from the Sun is shown for the four cones with angular radii of 30° , 45° , 60° and 90° . Again, no evidence of a CRE signal from the Sun is observed. Similar results are obtained when integral fluxes are analyzed.

1. Evaluation of statistical upper limits on the CRE flux from the Sun

As in §III A, our analysis in this case does not find evidence of a CRE signal from the Sun, and so we set statistical upper limits on solar CRE fluxes. Given a cone with angular radius $\Delta\Theta$ centered on the Sun, the observed counts $N_{real}(E|\Delta\Theta)$ in the energy bin E can be seen as a realization of a Poisson random variable. Assuming the hypothesis of a CRE signal from the Sun, these counts will be the sum of a signal contribution, $N_{Sun}(E|\Delta\Theta)$, plus a background contribution, $N_{bkg}(E|\Delta\Theta)$:

$$N_{real}(E|\Delta\Theta) = N_{Sun}(E|\Delta\Theta) + N_{bkg}(E|\Delta\Theta). \quad (15)$$

	$\Delta\Theta = 30^\circ$		$\Delta\Theta = 45^\circ$		$\Delta\Theta = 60^\circ$		$\Delta\Theta = 90^\circ$	
Energy (GeV)	Flux UL ($\text{GeV}^{-1}\text{m}^{-2}\text{s}^{-1}$)	Fractional UL	Flux UL ($\text{GeV}^{-1}\text{m}^{-2}\text{s}^{-1}$)	Fractional UL	Flux UL ($\text{GeV}^{-1}\text{m}^{-2}\text{s}^{-1}$)	Fractional UL	Flux UL ($\text{GeV}^{-1}\text{m}^{-2}\text{s}^{-1}$)	Fractional UL
60.4 – 68.2	$3.508 \cdot 10^{-6}$	0.008	$4.650 \cdot 10^{-6}$	0.005	$3.934 \cdot 10^{-6}$	0.002	$7.506 \cdot 10^{-6}$	0.002
68.2 – 77.4	$2.114 \cdot 10^{-6}$	0.007	$2.496 \cdot 10^{-6}$	0.004	$3.518 \cdot 10^{-6}$	0.003	$4.096 \cdot 10^{-6}$	0.002
77.4 – 88.1	$2.744 \cdot 10^{-6}$	0.013	$5.506 \cdot 10^{-6}$	0.012	$3.131 \cdot 10^{-6}$	0.004	$4.555 \cdot 10^{-6}$	0.003
88.1 – 101	$2.516 \cdot 10^{-6}$	0.019	$5.127 \cdot 10^{-6}$	0.018	$4.400 \cdot 10^{-6}$	0.009	$7.696 \cdot 10^{-6}$	0.008
101 – 116	$2.190 \cdot 10^{-6}$	0.024	$1.963 \cdot 10^{-6}$	0.010	$2.779 \cdot 10^{-6}$	0.008	$3.845 \cdot 10^{-6}$	0.006
116 – 133	$1.026 \cdot 10^{-6}$	0.017	$9.091 \cdot 10^{-7}$	0.007	$1.935 \cdot 10^{-6}$	0.009	$1.583 \cdot 10^{-6}$	0.004
133 – 154	$1.471 \cdot 10^{-6}$	0.039	$1.261 \cdot 10^{-6}$	0.015	$1.337 \cdot 10^{-6}$	0.010	$1.795 \cdot 10^{-6}$	0.006
154 – 180	$5.671 \cdot 10^{-7}$	0.021	$5.297 \cdot 10^{-7}$	0.009	$7.971 \cdot 10^{-7}$	0.008	$1.435 \cdot 10^{-6}$	0.007
180 – 210	$8.580 \cdot 10^{-7}$	0.054	$1.348 \cdot 10^{-6}$	0.039	$1.419 \cdot 10^{-6}$	0.025	$1.489 \cdot 10^{-6}$	0.013
210 – 246	$1.252 \cdot 10^{-6}$	0.133	$9.240 \cdot 10^{-7}$	0.045	$8.574 \cdot 10^{-7}$	0.024	$7.953 \cdot 10^{-7}$	0.011
246 – 291	$2.905 \cdot 10^{-7}$	0.049	$4.411 \cdot 10^{-7}$	0.034	$6.033 \cdot 10^{-7}$	0.027	$1.556 \cdot 10^{-6}$	0.036
291 – 346	$3.946 \cdot 10^{-7}$	0.111	$5.473 \cdot 10^{-7}$	0.073	$7.581 \cdot 10^{-7}$	0.059	$7.778 \cdot 10^{-7}$	0.030
346 – 415	$2.457 \cdot 10^{-7}$	0.115	$2.925 \cdot 10^{-7}$	0.064	$3.715 \cdot 10^{-7}$	0.048	$6.160 \cdot 10^{-7}$	0.040
415 – 503	$1.567 \cdot 10^{-7}$	0.140	$2.057 \cdot 10^{-7}$	0.085	$2.979 \cdot 10^{-7}$	0.072	$3.187 \cdot 10^{-7}$	0.038
503 – 615	$6.318 \cdot 10^{-8}$	0.094	$7.052 \cdot 10^{-8}$	0.049	$9.512 \cdot 10^{-8}$	0.041	$1.644 \cdot 10^{-7}$	0.037
615 – 772	$7.297 \cdot 10^{-8}$	0.251	$1.047 \cdot 10^{-7}$	0.169	$1.486 \cdot 10^{-7}$	0.134	$2.501 \cdot 10^{-7}$	0.111
772 – 1000	$6.097 \cdot 10^{-8}$	0.493	$5.951 \cdot 10^{-8}$	0.192	$9.720 \cdot 10^{-8}$	0.178	$2.088 \cdot 10^{-7}$	0.196

TABLE II: Statistical upper limits at 95% confidence level on the CRE flux asymmetries between the real and the fake Sun, evaluated in cones of angular radii $\Delta\Theta = 30^\circ, 45^\circ, 60^\circ, 90^\circ$. The upper limits are also expressed in terms of fractions of the CRE flux from the fake Sun.

Angular radius	Maximum deviation (S_{max})	$P(S_{max})$	$P(S > S_{max})$
30°	1.925	0.054	0.611
45°	0.419	0.675	1.000
60°	-0.654	0.513	1.000
90°	1.026	0.305	0.998

TABLE III: For each cone used for the flux asymmetry analysis the maximum deviation (either positive or negative) in terms of significance from the null value are shown with the corresponding probability of finding a larger significance value. The last column shows the probability of finding at least one energy bin a with larger flux asymmetry than the maximum observed value.

Both $N_{Sun}(E|\Delta\Theta)$ and $N_{bkg}(E|\Delta\Theta)$ can be seen as Poisson random variables. The only information available about $N_{Sun}(E|\Delta\Theta)$ is that, in the hypothesis of a CRE signal from the Sun, its average value (which is unknown) must be non-negative:

$$\langle N_{Sun}(E|\Delta\Theta) \rangle \geq 0. \quad (16)$$

On the other hand, the average value of $N_{bkg}(E|\Delta\Theta)$ can be estimated from the randomized data sets, and is given by:

$$\langle N_{bkg}(E|\Delta\Theta) \rangle = \alpha(E) N_{sim}(E|\Delta\Theta) \quad (17)$$

where $\alpha(E)$ is the ratio between the total real and simulated events in the energy bin E .

The goal of our analysis is to evaluate an upper limit on the average value $\langle N_{Sun}(E|\Delta\Theta) \rangle$, that will be converted

into an upper limit on the CRE flux from the Sun after properly taking into account the detector acceptance and the live time. For our calculation we implemented the Bayesian method with the assumption of a uniform prior density. The mathematical details of the method can be found in Ref. [27] (pp. 139-142).

Fig. 4 shows the statistical upper limits at different confidence levels on the CRE fluxes from different cones centered on the Sun and with angular radii ranging from 30° to 90° . The results are consistent with those shown in Fig. 2. In Table IV the values of the upper limits at 95% confidence level for the flux asymmetry $dA'_\Phi(E|\Delta\Theta)/dE$ in the different ROIs are summarized. The calculated upper limits are also expressed in terms of fractional excess with respect to the expected isotropic flux.

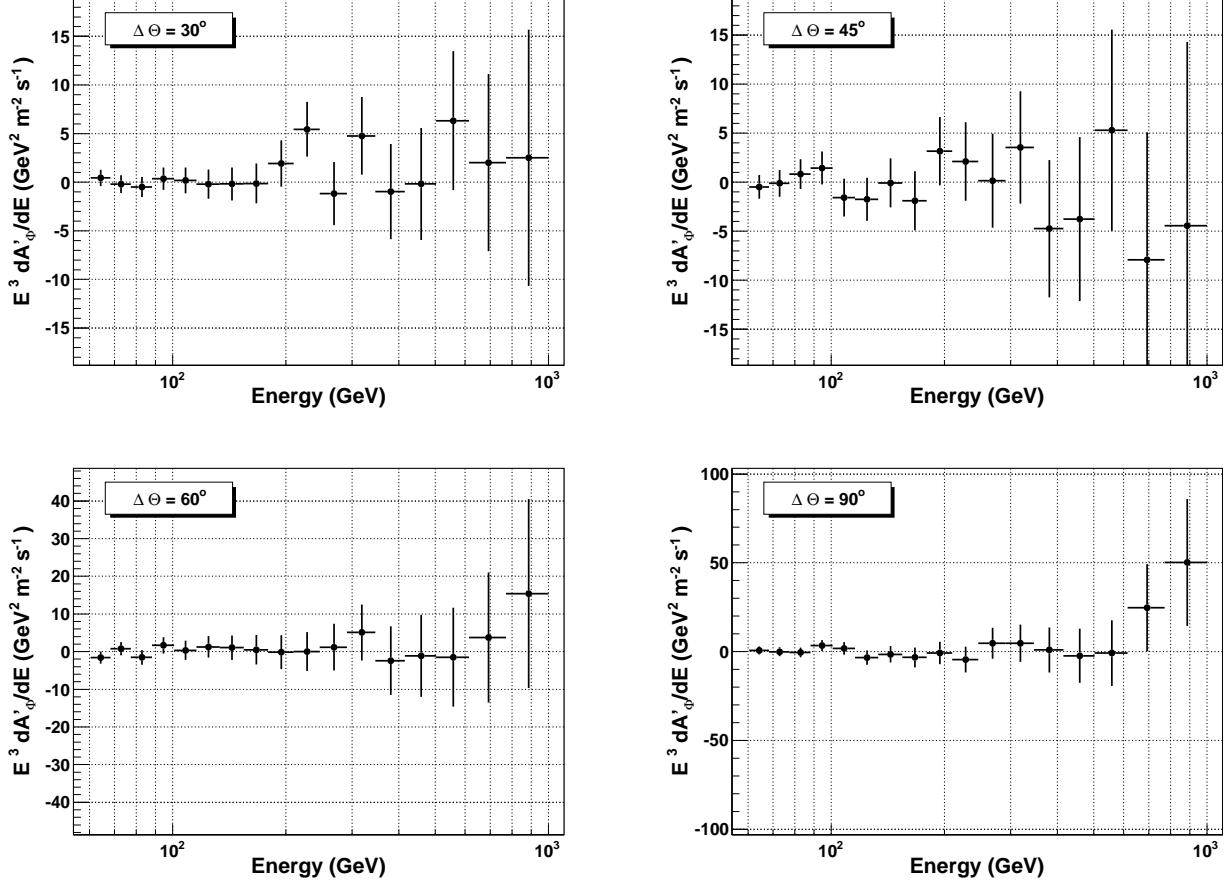


FIG. 3: Differential flux asymmetry between real and simulated events from the Sun evaluated in cones with angular radii $\Delta\Theta = 30^\circ$ (top left panel), 45° (top right panel), 60° (bottom left panel) and 90° (bottom right panel). Only statistical error bars are shown.

2. Spherical harmonics analysis

The previous analyses excluded variations of the CRE flux correlated from the Sun's direction. However, due to the effects of the heliospheric magnetic field and the geomagnetic field, a CRE signal from the Sun could produce a flux excess from a direction shifted with respect to the Sun's position. Also, since CREs from the Sun are expected to be spread over a cone with a finite angular radius, an excess of CREs from the Sun could induce an anisotropy on a large angular scale.

To investigate this possibility we implemented a more general analysis method, based on spherical harmonics analysis of a fluctuation sky map. This method was applied in Ref. [16] to search for anisotropies in the CRE flux in the Galactic reference frame, while in this paper we adopted the custom coordinates in Eq. 7 derived from the ecliptic reference frame.

The fluctuation sky map was built starting from the real sky map and from the simulated one, which was generated using the randomized data sets. The analysis was performed on sky maps of the counts integrated

above a given energy in order to retain sufficient statistics in each energy bin. The fluctuation in the i th pixel is:

$$f_i(> E) = \frac{N_{i,real}(> E) - \alpha N_{i,sim}(> E)}{\alpha N_{i,sim}(> E)}. \quad (18)$$

The fluctuation sky map is then expanded in the basis of spherical harmonics to obtain the set of coefficients a_{lm} . The coefficients of the angular power spectrum are given by the variance of the $2l+1$ a_{lm} coefficients at each multipole:

$$\hat{C}_l = \frac{1}{2l+1} \sum_{m=-l}^l |a_{lm}|^2 \quad (19)$$

Each coefficient \hat{C}_l characterizes the intensity of the fluctuations on an angular scale of $\sim 180^\circ/l$. In the case of an isotropic flux, each of the coefficients C_l can be seen as a random variable with a true value (white noise) given by:

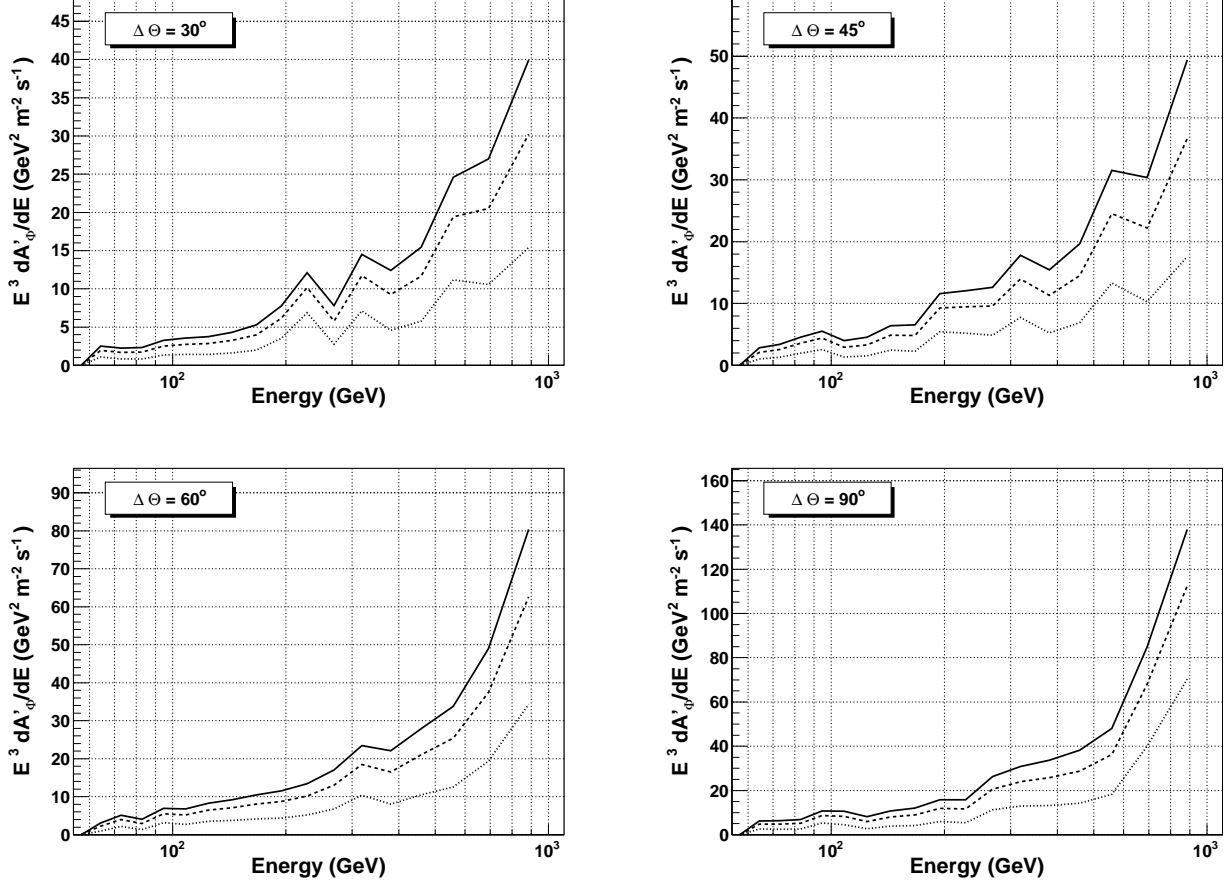


FIG. 4: Statistical upper limits at confidence levels of 68% (dotted lines), 95% (dashed lines) and 99% (continuous lines) for the CRE fluxes from the Sun, evaluated in cones with angular radii $\Delta\Theta = 30^\circ$ (top left panel), 45° (top right panel), 60° (bottom left panel) and 90° (bottom right panel).

$$C_l = C_N = \frac{4\pi}{N} \quad (20)$$

where N is the total number of observed events. The confidence intervals for the \hat{C}_l can be evaluated by noting that the random variable $(2l+1)\hat{C}_l/C_l$ follows a χ^2_{2l+1} distribution.

In Fig. 5 the angular power spectra after the subtraction of the white noise contribution C_N are shown for four different minimum energies (60 GeV, 100 GeV, 200 GeV and 500 GeV). The curves show the 3σ and 5σ probability intervals assuming the hypothesis of an isotropic CRE flux. All the data points lie within the 3σ interval, indicating that the measurements are consistent with the hypothesis of an isotropic CRE flux. Hence, we conclude that no preferred CRE arrival directions are observed.

IV. SOLAR CRE FLUXES FROM DARK MATTER

We now determine constraints on DM model parameters by comparing our upper limits on solar CRE fluxes to the predicted fluxes of the two DM annihilation scenarios considered in Ref. [1]: (1) capture of DM particles by the Sun via elastic scattering interactions and subsequent annihilation to e^\pm through an intermediate state ϕ , and (2) capture of DM particles by the Sun via inelastic scattering interactions and subsequent annihilation of the captured DM particles outside the Sun directly to e^\pm .

A. Dark matter annihilation through an intermediate state

In this case we assume the standard scenario for WIMP capture by the Sun, namely that DM particles χ are captured by the Sun through elastic scattering interactions and then continue to lose energy through subsequent

	$\Delta\Theta = 30^\circ$		$\Delta\Theta = 45^\circ$		$\Delta\Theta = 60^\circ$		$\Delta\Theta = 90^\circ$	
Energy (GeV)	Flux UL ($\text{GeV}^{-1}\text{m}^{-2}\text{s}^{-1}$)	Fractional UL	Flux UL ($\text{GeV}^{-1}\text{m}^{-2}\text{s}^{-1}$)	Fractional UL	Flux UL ($\text{GeV}^{-1}\text{m}^{-2}\text{s}^{-1}$)	Fractional UL	Flux UL ($\text{GeV}^{-1}\text{m}^{-2}\text{s}^{-1}$)	Fractional UL
60.4 – 68.2	$7.344 \cdot 10^{-6}$	0.017	$7.865 \cdot 10^{-6}$	0.008	$8.390 \cdot 10^{-6}$	0.005	$1.823 \cdot 10^{-5}$	0.006
68.2 – 77.4	$4.366 \cdot 10^{-6}$	0.015	$6.652 \cdot 10^{-6}$	0.010	$1.033 \cdot 10^{-5}$	0.009	$1.245 \cdot 10^{-5}$	0.006
77.4 – 88.1	$3.060 \cdot 10^{-6}$	0.015	$6.279 \cdot 10^{-6}$	0.014	$5.237 \cdot 10^{-6}$	0.007	$9.069 \cdot 10^{-6}$	0.006
88.1 – 101	$2.987 \cdot 10^{-6}$	0.022	$5.211 \cdot 10^{-6}$	0.018	$6.548 \cdot 10^{-6}$	0.013	$1.033 \cdot 10^{-5}$	0.010
101 – 116	$2.162 \cdot 10^{-6}$	0.023	$2.296 \cdot 10^{-6}$	0.012	$4.093 \cdot 10^{-6}$	0.012	$6.541 \cdot 10^{-6}$	0.010
116 – 133	$1.471 \cdot 10^{-6}$	0.025	$1.710 \cdot 10^{-6}$	0.013	$3.363 \cdot 10^{-6}$	0.015	$3.091 \cdot 10^{-6}$	0.007
133 – 154	$1.090 \cdot 10^{-6}$	0.029	$1.631 \cdot 10^{-6}$	0.020	$2.384 \cdot 10^{-6}$	0.017	$2.683 \cdot 10^{-6}$	0.010
154 – 180	$8.568 \cdot 10^{-7}$	0.033	$1.034 \cdot 10^{-6}$	0.019	$1.729 \cdot 10^{-6}$	0.018	$1.912 \cdot 10^{-6}$	0.010
180 – 210	$8.360 \cdot 10^{-7}$	0.052	$1.257 \cdot 10^{-6}$	0.037	$1.185 \cdot 10^{-6}$	0.020	$1.614 \cdot 10^{-6}$	0.014
210 – 246	$8.587 \cdot 10^{-7}$	0.087	$7.968 \cdot 10^{-7}$	0.038	$8.626 \cdot 10^{-7}$	0.024	$9.827 \cdot 10^{-7}$	0.014
246 – 291	$2.983 \cdot 10^{-7}$	0.050	$4.946 \cdot 10^{-7}$	0.038	$6.749 \cdot 10^{-7}$	0.031	$1.062 \cdot 10^{-6}$	0.024
291 – 346	$3.630 \cdot 10^{-7}$	0.100	$4.318 \cdot 10^{-7}$	0.056	$5.716 \cdot 10^{-7}$	0.043	$7.422 \cdot 10^{-7}$	0.028
346 – 415	$1.681 \cdot 10^{-7}$	0.074	$2.048 \cdot 10^{-7}$	0.043	$2.997 \cdot 10^{-7}$	0.038	$4.661 \cdot 10^{-7}$	0.030
415 – 503	$1.205 \cdot 10^{-7}$	0.103	$1.504 \cdot 10^{-7}$	0.060	$2.176 \cdot 10^{-7}$	0.051	$2.979 \cdot 10^{-7}$	0.035
503 – 615	$1.113 \cdot 10^{-7}$	0.184	$1.409 \cdot 10^{-7}$	0.108	$1.457 \cdot 10^{-7}$	0.066	$2.082 \cdot 10^{-7}$	0.047
615 – 772	$6.154 \cdot 10^{-8}$	0.197	$6.662 \cdot 10^{-8}$	0.098	$1.125 \cdot 10^{-7}$	0.097	$2.038 \cdot 10^{-7}$	0.088
772 – 1000	$4.344 \cdot 10^{-8}$	0.286	$5.276 \cdot 10^{-8}$	0.162	$9.005 \cdot 10^{-8}$	0.161	$1.617 \cdot 10^{-7}$	0.145

TABLE IV: Statistical upper limits at 95% confidence level on the CRE flux asymmetries between the real and the simulated Sun, generated by the event shuffling technique, evaluated in cones of angular radii $\Delta\Theta = 30^\circ, 45^\circ, 60^\circ, 90^\circ$. The upper limits are also expressed in terms of fractions of the isotropic CRE flux from the simulated Sun.

scatterings, eventually thermalizing and sinking to the core where they annihilate. In general, the only annihilation products which can escape the Sun are neutrinos; photons and charged particle final states are trapped by interactions with the dense matter in the Sun. However, recently scenarios have been proposed in which DM particles annihilate into a light intermediate state ϕ , i.e., $\chi\chi \rightarrow \phi\phi$, with the ϕ subsequently decaying to standard model particles; these models have been suggested to provide a means of explaining an excess in the CRE spectrum reported by ATIC and *Fermi* and in the positron fraction reported by PAMELA by DM annihilation or decay [29–35]. For the case considered in Ref. [1], the ϕ are assumed to be able to escape the Sun without further interactions, with each ϕ decaying to an e^\pm pair. If this decay happens outside the surface of the Sun, the e^\pm could reach the Earth and may be detectable in the form of an observed excess of CREs from the direction of the Sun.

The DM particles are assumed to annihilate at rest in the core of the Sun, so in the lab frame the energy of the ϕ , E_ϕ , is equal to the DM particle mass m_χ . We assume ϕ to be a light scalar such that $m_\phi \ll m_\chi$, hence the ϕ are relativistic. The energy of the ϕ is described by the parameter $\beta_{\text{cl}} = v_{\text{cl}}/c$ where v_{cl} is the relative velocity of the lab frame and the ϕ rest frame (hereafter, the CM frame). The ϕ are assumed to lose a negligible amount of energy exiting the Sun. A ϕ decays into an e^\pm pair with an isotropic angular distribution in the CM frame. Both the e^+ and e^- have the same energy in the CM

frame, parameterized by $\beta_{jc} = v_{jc}/c = \sqrt{1 - (4m_e^2/m_\phi^2)}$, where m_e is the electron mass and v_{jc} is the velocity of particle j (the electron or positron) in the CM frame. However, in the lab frame the e^\pm are boosted and so the angular distribution is no longer isotropic, and the energy of an e^\pm in the lab frame depends on the angle at which it is emitted relative to the direction in which the ϕ is traveling. In the lab frame the angle at which the e^\pm is emitted is denoted θ_{lab} ; in the CM frame it is θ_{cm} . The e^\pm are assumed to travel in straight lines and to suffer no energy losses before reaching the detector, i.e., the effects of magnetic fields are assumed to be negligible.

The flux of e^\pm per time, area, and energy per cosine of the detector angle from the direction θ_{det} is given by integrating the differential rate of decay of ϕ along the line of sight in the direction of θ_{det} ,

$$\frac{dN}{dt dA d\cos\theta_{\text{det}} dE_{\text{det}}}(\theta_{\text{det}}, E_{\text{det}}) = \int_0^\infty dR \frac{dN}{dV dt} \frac{d\Gamma}{d\cos\theta_{\text{det}}} \delta(E_{\text{det}} - E), \quad (21)$$

where R is the distance from the detector in the line-of-sight direction defined by θ_{det} . At each θ_{det} we exclude the contribution from ϕ decays occurring in the range of R within the surface of the Sun.

The first term in Eq. 21 is the rate of production of e^\pm (equal to twice the rate of ϕ decays) per volume at a volume element a distance r from the center of the Sun, and is given by

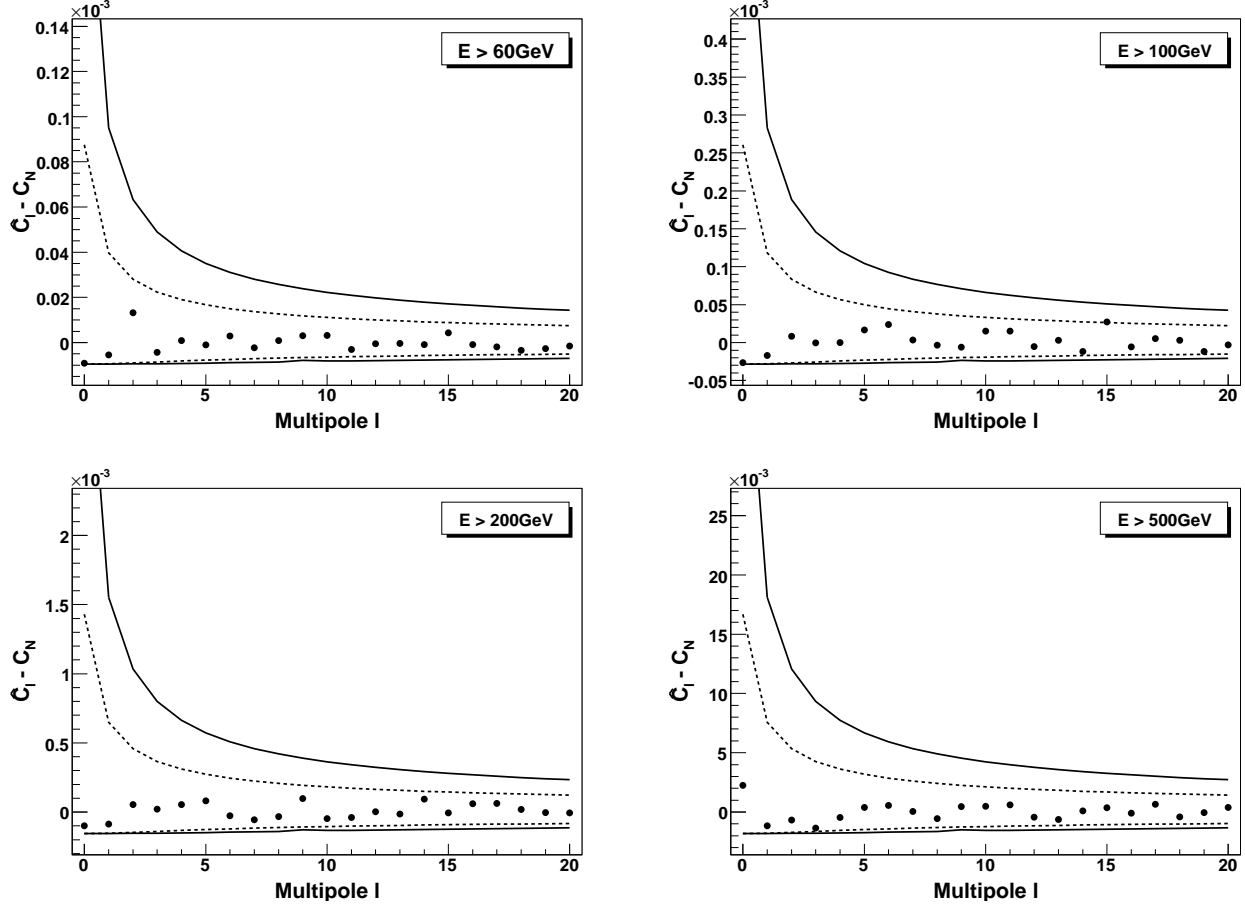


FIG. 5: Angular power spectra for different minimum energies: 60 GeV (top left panel), 100 GeV (top right panel), 200 GeV (bottom left panel), 500 GeV (bottom right panel). The points show the quantities $\hat{C}_l - C_N$. The dashed lines and the continuous lines show respectively the 3σ and 5σ intervals for the probability distribution of the white noise.

$$\frac{dN}{dV dt}(r(\theta_{\text{det}}, R)) = 2 \frac{C_{\odot} e^{-r/L}}{4\pi r^2 L} \quad (22)$$

where C_{\odot} is the capture rate of DM particles in the Sun and the characteristic decay length $L \equiv \gamma_{\text{cl}} c \tau$, where $\gamma_{\text{cl}} = \gamma(\beta_{\text{cl}})$ with $\gamma(\beta) = 1/\sqrt{1-\beta^2}$ and τ is the lifetime of the ϕ . Equilibrium is assumed, i.e., for every two DM particles that are captured, two annihilate, so C_{\odot} also represents the rate of production of ϕ particles by annihilation at the center of the Sun. For the range of scattering cross-sections considered here, the capture rate is in general sufficiently large that equilibrium is a valid assumption, although we discuss this issue in greater detail when presenting our constraints.

We consider separately the cases of solar capture by spin-independent scattering and spin-dependent scattering. Using DarkSUSY [36], we calculate the capture rate via elastic scattering C_{\odot} as a function of m_{χ} . A Maxwell-Boltzmann velocity distribution is assumed, with the solar velocity relative to the DM rest frame $v_{\odot} = 220$ km/s, the DM velocity dispersion $\tilde{v} = 270$ km/s, and the lo-

cal DM density $\rho_{\text{DM}} = 0.3$ GeV/cm³. For the case of spin-independent scattering we set the spin-dependent scattering cross-section $\sigma_{\text{SD}} = 0$ cm² and calculate the capture rates for $\sigma_{\text{SI}} = 10^{-43}$ cm²; for spin-dependent scattering we set $\sigma_{\text{SI}} = 0$ cm² and calculate the capture rates for $\sigma_{\text{SD}} = 10^{-40}$ cm². The reference values of σ_{SI} and σ_{SD} roughly correspond to the current experimental upper limits on these parameters. For the range of parameters considered here the capture rate scales linearly with σ_{SD} and σ_{SI} .

The second term in Eq. 21 is the angular distribution of the e^{\pm} from the decay of a ϕ , as observed in the lab frame, and expressed in terms of detector angle,

$$\frac{d\Gamma}{d\cos\theta_{\text{det}}} = \frac{d\Gamma}{d\cos\theta_{\text{cm}}} \left| \frac{d\cos\theta_{\text{cm}}}{d\cos\theta_{\text{lab}}} \right| \frac{d\cos\theta_{\text{lab}}}{d\cos\theta_{\text{det}}}. \quad (23)$$

In the rest frame of the ϕ the decays are isotropic, so, after integrating over the azimuthal angle we can write

$$\frac{d\Gamma}{d\cos\theta_{\text{cm}}} = -1/2. \quad (24)$$

The transformation between the CM angle and lab angle is given by [37]

$$\left| \frac{d \cos \theta_{\text{cm}}}{d \cos \theta_{\text{lab}}} \right| = \frac{[\gamma_{\text{cl}}^2 (\alpha + \cos \theta_{\text{cm}})^2 + \sin^2 \theta_{\text{cm}}]^{3/2}}{|\gamma_{\text{cl}} (1 + \alpha \cos \theta_{\text{cm}})|}, \quad (25)$$

with $\gamma_{\text{cl}} = \gamma(\beta_{\text{cl}})$ and $\alpha = \beta_{\text{cl}}/\beta_{\text{jc}}$. The lab and detector angles are related by

$$\theta_{\text{lab}} = \theta_{\text{det}} + \sin^{-1} \left(\frac{R \sin \theta_{\text{det}}}{r} \right), \quad (26)$$

which gives

$$\frac{d \cos \theta_{\text{lab}}}{d \cos \theta_{\text{det}}} = \frac{(|D_{\odot} - R \cos(\theta_{\text{det}})| + R \cos(\theta_{\text{det}}))^2}{r |D_{\odot} - R \cos(\theta_{\text{det}})|}. \quad (27)$$

The delta function in Eq. 21 enforces that the energy observed at the detector is equal to the energy of the emitted e^{\pm} boosted to the lab frame,

$$E(\theta_{\text{cm}}) = \frac{1}{2} \gamma_{\text{cl}} m_{\phi} (1 + \beta_{\text{cl}} \cos \theta_{\text{cm}}). \quad (28)$$

Note that because the energy in the lab frame depends only on θ_{cm} , and because θ_{lab} is determined by θ_{cm} , fixing E_{det} corresponds to selecting only CREs emitted at the corresponding θ_{lab} . For a specified θ_{det} , the θ_{lab} of particles observed along the line-of-sight R varies, hence the observed energy of CREs emitted from a point along the line-of-sight is a function of R , i.e., $E_{\text{det}}(R)$. We rewrite the delta function in Eq. 21 as the composition

$$\delta(E_{\text{det}} - E(R)) = \frac{\delta(R - R_0)}{\frac{dE}{dR}(R_0)} \quad (29)$$

and then perform the integration over R . The parameter R_0 is the value of R along the line-of-sight in the direction θ_{det} where θ_{lab} takes the value required to generate CREs with a given E_{det} .

We evaluate the CRE flux within a ROI of 30° centered on the Sun, and fix the value of $m_{\phi} = 1 \text{ GeV}$. We calculate limits for three values of the decay length $L = 5 \text{ AU}$, 1 AU , and 0.1 AU . Decreasing L increases the observed CRE flux by condensing the region within which most ϕ decay. However, we emphasize that even for as large a decay length as $L = 5 \text{ AU}$, the signal in the energy range used in this analysis is strongly peaked in the direction of the Sun and extends only a few degrees at most. Since the ϕ in this scenario are relativistic, in the lab frame the emitted e^{\pm} are boosted along the direction the ϕ is moving, and so only ϕ exiting the Sun very close to the direction of the detector will produce decay products with large enough θ_{lab} to reach the detector. In particular, for the e^{\pm} to have sufficient

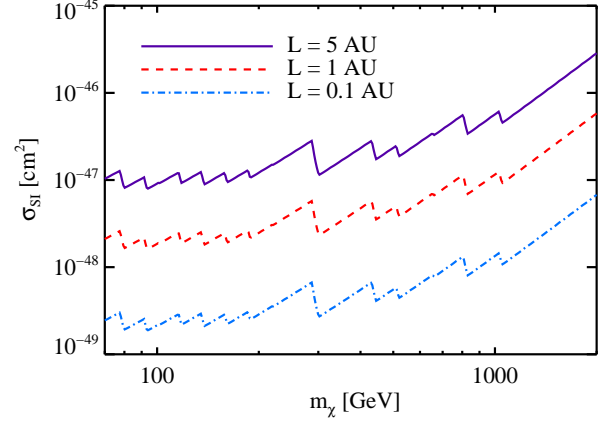


FIG. 6: Constraints on DM annihilation to e^+e^- via an intermediate state, from solar CRE flux upper limits. Solar capture of DM is assumed to take place via spin-independent scattering. The constraints obtained for three values of the decay length L of the intermediate state are shown. Models above the curves exceed the solar CRE flux upper limit at 95% CL for a 30° ROI centered on the Sun.

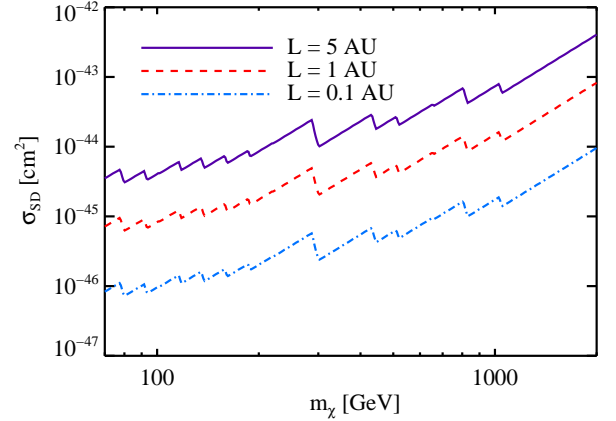


FIG. 7: Constraints on DM parameters for annihilation to e^+e^- via an intermediate state as in Fig. 6, except assuming solar capture by spin-dependent scattering.

energy to fall within the energy range of this analysis, a significant fraction of the ϕ energy must be deposited into the e^{\pm} that reach the detector. This only occurs for e^{\pm} emitted with very small θ_{lab} . This also leads to an energy dependence of the angular signal: for a given DM scenario, the angular extent of the flux at high energies is smaller than at lower energies. We note that decreasing m_{ϕ} for a fixed m_{χ} narrows the angular extent of the signal, and therefore has little impact on our results. We confirmed that for m_{ϕ} as large as 10 GeV , the cross-section limits vary negligibly except for a slight weakening of the limit at the lowest end of the m_{χ} range considered here.

Figs. 6 and 7 show the constraints on σ_{SI} and σ_{SD} as a function of m_χ , derived from the upper limits on the solar CRE flux obtained in §III B. For each m_χ the CRE flux in each energy bin used in this analysis was calculated, and the limit on the scattering cross-section was set by the energy bin providing the strongest constraint. The jagged shape of the curve reflects the transitions between the energy bins setting the strongest limit. Models above the curves exceed the 95% CL solar CRE flux upper limit for the 30° ROI in at least one energy bin. Ref. [1] notes that due to the Parker spiral shape of the Sun's magnetic field, CREs emitted from the Sun may be deflected in such a way as to appear to originate from a source displaced by up to 30° from the Sun's position. If we instead consider larger ROIs centered on the Sun in order to accommodate the expected angular distribution of the flux of a displaced source, the constraints derived on the scattering cross-sections would be weakened by $\sim 30\%$ using the flux upper limit for the 45° ROI, or by a factor of ~ 2 if the 60° ROI flux upper limit were used.

The bounds on the scattering cross-sections we derive for e^\pm final states are significantly below the typical constraints from direct detection experiments, and so we are prompted to examine more closely the validity of our assumption of equilibrium. For the limiting values we derive on elastic scattering cross-sections, capture and annihilation are effectively in equilibrium assuming an annihilation cross-section consistent with thermal relic dark matter $\langle\sigma v\rangle = 3 \times 10^{-26} \text{ cm}^3 \text{ s}^{-1}$ for all values of the decay length L considered here. In particular, for the limiting values of the scattering cross-sections the flux suppression relative to the equilibrium flux for any mass we consider is always less than 3% (following the standard calculation implemented in Ref. [36]), and thus we work under the assumption of equilibrium, noting that there remain uncertainties in the capture rate calculation at the level of a factor of a few (e.g., [38]).

Decays to e^\pm are generally accompanied by final state radiation (FSR), so these scenarios can also be constrained by solar gamma-ray observations. Ref. [39] derived bounds on the rate of decay to e^\pm by requiring that the predicted FSR does not exceed the solar gamma-ray emission measured by *Fermi*. However, the constraints we obtained on the elastic scattering cross-sections from the solar CRE flux correspond to constraints on the annihilation rate roughly 2-4 orders of magnitude stronger than those placed by gamma-ray constraints on FSR. The strength of the CRE limits relative to those from FSR increases for larger m_χ . The relative strength of the constraints derived from the CRE flux limits compared to those from the gamma-ray measurements can be attributed in part to the fact that the FSR flux produced by annihilation to e^+e^- is ~ 2 -3 orders of magnitude smaller than the CRE flux. FSR emission also must compete with a known background gamma-ray flux from the Sun [40]. Furthermore, the FSR constraints in Ref. [39] were derived using the preliminary *Fermi* measurement of the solar spectrum which extends only

to 10 GeV, while this analysis spans CRE energies from 60 GeV to ~ 1 TeV. Since the FSR photon spectrum is harder than the measured solar gamma-ray spectrum, the strongest constraints are obtained from the highest energy bin in that analysis. Due to the fact that the FSR spectrum associated with the DM mass range considered in this analysis extends substantially higher than 10 GeV, the existing FSR constraints are significantly less competitive than our CRE constraints. A measurement of the solar gamma-ray emission at higher energies could likely strengthen the FSR constraints to some extent.

B. Inelastic dark matter

We now consider the flux of e^\pm from annihilation of DM particles captured by the Sun but with orbits which take them outside the surface of the Sun. In a standard WIMP scenario, DM particles captured by the Sun via elastic scattering quickly undergo subsequent scatterings which cause them to settle to the core, and hence the fraction of captured DM particles outside the surface of the Sun at any given time is negligible [38]. However, this is not necessarily the case for inelastic dark matter (iDM) [3, 41, 42]. This class of models has garnered interest recently in light of claims that iDM could naturally explain such observations as the 511 keV line observed by INTEGRAL/SPI [42] and the apparently inconsistent results of DAMA/LIBRA and CDMS if the DM scattered inelastically and thereby transitioned to an excited state with a slightly heavier mass.

For a DM particle χ to scatter inelastically off a nucleon N via the process $\chi + N \rightarrow \chi^* + N$, the DM must have energy $E \geq \delta(1 + m_\chi/m_N)$, where $\delta = m_{\chi^*} - m_\chi$. Particles captured by the sun by inelastic scattering typically lose enough energy after only a few interactions to prevent further energy loss by scattering. If the elastic scattering cross-section is sufficiently small ($\sigma_n \lesssim 10^{-47} \text{ cm}^2$, e.g., Ref. [1]), the captured particles will be unable to thermalize and settle to the core, and instead will remain on relatively large orbits. As a result, the density of captured DM particles outside the Sun may not be negligible in an iDM scenario, and the annihilation of those particles to e^\pm could thus produce an observable flux of CREs from the direction of the Sun. While it is not necessary for DM to annihilate primarily to e^\pm in order to explain the direct detection results (since direct detection experiments are not sensitive to the dominant annihilation channels), leptophilic iDM is strongly motivated since it could provide a consistent interpretation of multiple data sets [3, 42–44].

In the following we will assume that the DM particles annihilate at rest and thus the energy of the e^\pm produced in annihilation is well-approximated by $E_{\text{CRE}} = m_\chi$. We will further assume that the CREs suffer no significant energy losses between production at the surface of the Sun and arrival at the detector, and so we expect a mono-

energetic flux of CREs in this scenario.

For simplicity, we assume all annihilations occur at the surface of the Sun (as in [1]), since the density of DM falls off quickly with distance from the Sun. Naturally, e^\pm produced in annihilations inside the surface of the Sun cannot escape the Sun, and thus do not produce a detectable flux.

The isotropic flux of e^\pm particles from the Sun is

$$F = 2 \frac{\Gamma_{A,\text{out}}}{4\pi D_\odot^2} \quad (30)$$

where $\Gamma_{A,\text{out}}$ is the annihilation rate of DM particles outside the surface of the Sun. The factor of 2 accounts for the fact that 2 CREs are emitted per annihilation of a pair of DM particles. However, it is also necessary to take into account that CREs produced on the surface of the Sun opposite to the Earth are extremely unlikely to reach the detector, so we assume the flux of CREs *observable* at the detector is a factor of 2 smaller than that given by Eq. 30.

Following Refs. [45, 46], we assume that capture and annihilation of particles in this scenario is in equilibrium, i.e., $\Gamma_A = \frac{1}{2}C_\odot$, where Γ_A is the total annihilation rate at all radii. We emphasize, however, that due to significant uncertainties in the density profile of the captured iDM particles, the assumption of equilibrium is less robust in this case than in the elastic scattering scenario. Ref. [45] concludes that equilibrium will be attained, but notes the sizable uncertainties in this calculation. On the other hand, for the limiting cross-sections we determine for this scenario, the condition for equilibrium given in Ref. [46] for inelastic capture requires a minimum annihilation cross-section ranging from more than an order of magnitude smaller than for a thermal relic for small masses and $\delta = 110$ keV to a factor of ~ 3 larger than thermal for larger masses and $\delta = 140$ keV. In light of the uncertainties in this calculation, we again work under the assumption of equilibrium when deriving limits on the scattering cross-section.

Defining f_{out} as the fraction of captured DM particles outside the Sun at a given instant, we have

$$\Gamma_{A,\text{out}} = f_{\text{out}}\Gamma_A = \frac{1}{2}f_{\text{out}}C_\odot. \quad (31)$$

The capture rate of iDM particles by the Sun C_\odot was calculated by Refs. [45, 46]. Both studies note that there are uncertainties in this calculation at the factor of a few level. We use the capture rate as a function of DM mass m_χ and mass splitting δ as given in Fig. 2 of Ref. [46], and interpolate the results shown in that figure. The capture rates were calculated assuming the following parameters: the velocity of the Sun in the DM rest frame $v_\odot = 250$ km/s, the DM velocity dispersion $\tilde{v} = 250$ km/s, the local DM density $\rho_{\text{DM}} = 0.3$ GeV/cm³, and the cross-section per nucleon in the elastic limit $\sigma_0 = 10^{-40}$ cm². The relation between the total inelastic scattering cross-section and the total elastic scattering cross-section is given in Eq. 7 of Ref. [46]. The capture rate scales linearly

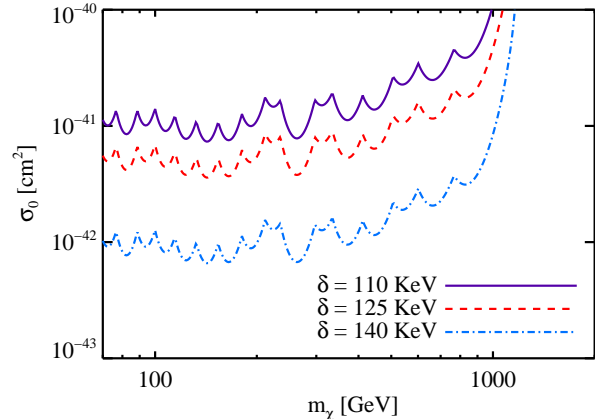


FIG. 8: Constraints on iDM model parameters for three values of the mass splitting δ . Models above the curves produce a solar CRE flux that exceeds the 95% CL flux upper limit for a 30° ROI centered on the Sun in one or more energy bins.

with ρ_{DM} and σ_0 , while the dependence on v_\odot and \tilde{v} is mild over the mass range of interest ($m_\chi \sim 100$ GeV to ~ 1 TeV). We note, however, that the constraints obtained by direct detection experiments may be more sensitive to variations in the assumed velocity distribution of the DM particles.

The parameter f_{out} was calculated by Ref. [1] by simulating the capture of DM particles by the Sun via inelastic scattering. Here we interpolate the values of f_{out} as a function of δ shown in Fig. 4 of that work, which were calculated for $m_\chi = 1$ TeV. Those authors note that the dependence on m_χ is weak for the mass range of interest, thus we adopt the values of f_{out} determined by [1] for $m_\chi = 1$ TeV for all masses considered. We caution that the calculation of f_{out} is subject to severe uncertainties, and a detailed study beyond the scope of this work is needed to more robustly estimate the value of this parameter. In particular, we note that f_{out} varies by more than an order of magnitude over the range of δ values considered in this study, and we therefore stress that the calculation of f_{out} introduces uncertainties in the derived scattering cross-section limits of at least a factor of a few.

We calculate the flux of CREs from annihilation of DM in this scenario as a function of m_χ and σ_0 for three values of the parameter δ . We then derive constraints on the m_χ - σ_0 parameter space by requiring that the predicted flux of each DM model does not exceed the 95% CL upper limits on solar CRE fluxes for a 30° ROI centered on the Sun, again using the results derived in §III B. Since the region from which the DM-induced flux originates in this scenario is the angular extent of the Sun, the 30° ROI is more than sufficient to encompass all of the DM signal.

The predicted flux is mono-energetic, however the finite energy resolution of the LAT will result in the observed events being assigned to more than one energy

bin. Since this may have a non-negligible impact on the derived scattering cross-section limits for DM masses near the energy bin edges, we convolve the predicted signal from each model with the energy resolution of the LAT and calculate its flux in each energy bin used in the analysis. We approximate the energy dispersion of the LAT as a Gaussian with σ given by the half-width of the 68% containment window (see Fig. 9 of [7]). For the energy range considered here the energy resolution ranges from $\sim 5\%$ to $\sim 14\%$. The cross-section limit at each mass is obtained from the energy bin providing the strongest constraint.

Fig. 8 shows the constraints from the solar CRE flux upper limits on iDM models in the m_χ - σ_0 parameter space for three values of δ . Models in the regions above the curves exceed the 95% CL flux upper limit for the 30° ROI in at least one energy bin. The rounded shape of the curves is due to accounting for the energy resolution of the LAT. These limits exclude the regions of parameter space compatible with the results of DAMA/LIBRA and CDMS (in addition to several other direct detection experiments) as determined by Ref. [11] for $\delta = 120$ keV, for the range of masses accessible to our analysis ($m_\chi \gtrsim 70$ GeV), assuming the dominant annihilation channel is e^\pm . Models consistent with both DAMA/LIBRA and CDMS at 90% CL exist for values of δ ranging from ~ 85 keV to ~ 135 keV [11]; for masses from 70 GeV to 250 GeV the range of allowed scattering cross-sections is from $\sigma_0 \sim 10^{-40} \text{ cm}^2$ to $\sigma_0 \sim 10^{-39} \text{ cm}^2$ [12]. Although the uncertainties in the calculation of the DM fluxes in this scenario are significant, we emphasize that constraining $\sigma_0 \lesssim 10^{-40} \text{ cm}^2$ is sufficient to exclude the cross-sections of models consistent with both data sets. The bounds we derive exclude the relevant cross-sections by 1-2 orders of magnitude, and hence we conclude that the parameter space of models preferred by DAMA/LIBRA can be confidently ruled out for $m_\chi \gtrsim 70$ GeV for annihilation to e^\pm despite the uncertainties in the flux calculation.

This analysis constrains DM models in which the primary annihilation channel is to e^\pm . We emphasize that although other annihilation channels can be probed by gamma-ray [39, 43, 47] or neutrino [39, 45, 46] measurements, the upper limits on solar CRE fluxes provide a uniquely strong constraint on the e^\pm final state, which is inaccessible to neutrino telescopes since no neutrinos are produced for this annihilation channel.

V. CONCLUSIONS

We used a sample of about 1.3×10^6 CRE events with energies above 60 GeV detected by the *Fermi* LAT during its first year of data-taking to search for flux excesses or deficits correlated with the Sun's direction.

Two analysis approaches were implemented, and neither yielded evidence of an enhancement in the CRE flux from the direction of the Sun. This result agrees with the more general one shown in Ref. [16], where no evidence of anisotropies was found in CRE arrival directions above 60 GeV in the Galactic reference frame.

We derived limits on DM models which generate a CRE flux from the Sun's direction for the two scenarios discussed in Ref. [1]. In the case of annihilation of DM through an intermediate state and subsequent decay to e^\pm , the upper limits on solar CRE fluxes provide significantly stronger constraints on the DM scattering cross-section than limits previously derived by constraining the FSR emission associated with this decay channel using solar gamma-ray measurements. For the iDM scenario, the solar CRE flux upper limits exclude the range of models which can reconcile the data from DAMA/LIBRA and CDMS for $m_\chi \gtrsim 70$ GeV, assuming DM annihilates predominantly to e^\pm . Since direct detection experiments are not sensitive to the dominant annihilation channels of the DM particles, other data, e.g., solar gamma-ray measurements and neutrino searches, may be able to further constrain these models by excluding regions of parameter space for alternative annihilation channels.

Acknowledgments

The *Fermi* LAT Collaboration acknowledges generous ongoing support from a number of agencies and institutes that have supported both the development and the operation of the LAT as well as scientific data analysis. These include the National Aeronautics and Space Administration and the Department of Energy in the United States, the Commissariat à l'Energie Atomique and the Centre National de la Recherche Scientifique / Institut National de Physique Nucléaire et de Physique des Particules in France, the Agenzia Spaziale Italiana and the Istituto Nazionale di Fisica Nucleare in Italy, the Ministry of Education, Culture, Sports, Science and Technology (MEXT), High Energy Accelerator Research Organization (KEK) and Japan Aerospace Exploration Agency (JAXA) in Japan, and the K. A. Wallenberg Foundation, the Swedish Research Council and the Swedish National Space Board in Sweden.

Additional support for science analysis during the operations phase is gratefully acknowledged from the Istituto Nazionale di Astrofisica in Italy and the Centre National d'Études Spatiales in France.

The authors thank Joakim Edsjö for his valuable contribution during the preparation of this manuscript.

JSG thanks J. Beacom, B. Dasgupta, S. Horiuchi, D. Malyshev, and I. Yavin for helpful discussions.

[1] P. Schuster, N. Toro, N. Weiner *et al.*, Phys. Rev. **D82**, 115012 (2010). [arXiv:0910.1839 [hep-ph]].

[2] M. Pospelov, A. Ritz and M. B. Voloshin, *Phys. Lett.*

- B662** (2008), 53. [arXiv:0711.4866 [hep-ph]].
- [3] N. Arkani-Hamed, D. P. Finkbeiner, T. R. Slatyer and N. Weiner, *Phys. Rev.* **D79** (2009), 015014. [arXiv:0810.0713 [hep-ph]].
- [4] O. Adriani *et al.* [PAMELA Collaboration], *Nature* **458**, 607 (2009) [arXiv:0810.4995 [astro-ph]].
- [5] J. Chang, J. H. Adams, H. S. Ahn *et al.*, *Nature* **456**, 362-365 (2008).
- [6] A. A. Abdo *et al.* [Fermi LAT Collaboration], *Phys. Rev. Lett.* **102**, 181101 (2009). [arXiv:0905.0025 [astro-ph.HE]].
- [7] M. Ackermann *et al.* [Fermi LAT Collaboration], *Phys. Rev.* **D82**, 092004 (2010). [arXiv:1008.3999 [astro-ph.HE]].
- [8] R. Bernabei *et al.* [DAMA Collaboration], *Eur. Phys. J.* **C56**, 333-355 (2008). [arXiv:0804.2741 [astro-ph]].
- [9] R. Bernabei, P. Belli, F. Cappella *et al.*, *Eur. Phys. J.* **C67**, 39-49 (2010). [arXiv:1002.1028 [astro-ph.GA]].
- [10] Z. Ahmed *et al.* [CDMS II Collaboration], *Science* **327**, 1619-1621 (2010). [arXiv:0912.3592 [astro-ph.CO]].
- [11] Z. Ahmed *et al.* [CDMS II Collaboration], [arXiv:1012.5078 [astro-ph.CO]].
- [12] S. Chang, G. D. Kribs, D. Tucker-Smith *et al.*, *Phys. Rev.* **D79**, 043513 (2009). [arXiv:0807.2250 [hep-ph]].
- [13] D. P. Finkbeiner, T. Lin, N. Weiner, *Phys. Rev.* **D80**, 115008 (2009). [arXiv:0906.0002 [astro-ph.CO]].
- [14] C. Savage, G. Gelmini, P. Gondolo *et al.*, *JCAP* **0904**, 010 (2009). [arXiv:0808.3607 [astro-ph]].
- [15] W. B. Atwood *et al.* [Fermi LAT Collaboration], *Astrophys. J.* **697**, 1071-1102 (2009). [arXiv:0902.1089 [astro-ph.IM]].
- [16] M. Ackermann *et al.* [Fermi LAT Collaboration], *Phys. Rev.* **D82**, 092003 (2010). [arXiv:1008.5119 [astro-ph.HE]].
- [17] <http://www.ngdc.noaa.gov/IAGA/vmod/igrf.html>.
- [18] J. P. Roberts, arXiv:1005.4668 [astro-ph.HE].
- [19] E. Orlando and A. W. Strong, *Astron. Astrophys.* **480**, 847 (2008) [arXiv:0801.2178 [astro-ph]].
- [20] R. Schlickeiser and J. Ruppel, *New J. Phys.* **12**, 033044 (2010) [arXiv:0908.2183 [astro-ph.HE]].
- [21] E. N. Parker, *Astrophys. J.* **128**, 664 (1958).
- [22] G. B. Rybicki, A. P. Lightman, "Radiative Processes in Astrophysics", Wiley-VCH (1979)
- [23] P. Duffett-Smith, "Practical astronomy with your calculator", Third Edition, Cambridge University Press (1988)
- [24] <http://iau-comm4.jpl.nasa.gov/access2ephis.html>.
- [25] K. M. Gorski, E. Hivon, A. J. Banday *et al.*, *Astrophys. J.* **622**, 759-771 (2005). [astro-ph/0409513]. <http://healpix.jpl.nasa.gov>
- [26] G. D'Agostini *Nucl. Inst. Meth.* **A364**, 306 (1994).
- [27] G. Cowan, "Statistical data analysis", Oxford University Press (1998)
- [28] T. -P. Li, Y. -Q. Ma, *Astrophys. J.* **272**, 317-324 (1983).
- [29] M. Pospelov, A. Ritz, *Phys. Lett.* **B671**, 391-397 (2009). [arXiv:0810.1502 [hep-ph]].
- [30] I. Cholis, G. Dobler, D. P. Finkbeiner *et al.*, *Phys. Rev.* **D80**, 123518 (2009). [arXiv:0811.3641 [astro-ph]].
- [31] I. Cholis, D. P. Finkbeiner, L. Goodenough *et al.*, *JCAP* **0912**, 007 (2009). [arXiv:0810.5344 [astro-ph]].
- [32] M. Kuhlen, D. Malyshev, *Phys. Rev.* **D79** (2009) 123517. [arXiv:0904.3378 [hep-ph]].
- [33] L. Bergstrom, J. Edsjo, G. Zaharijas, *Phys. Rev. Lett.* **103**, 031103 (2009). [arXiv:0905.0333 [astro-ph.HE]].
- [34] D. Grasso *et al.* [FERMI-LAT Collaboration], *Astropart. Phys.* **32**, 140-151 (2009). [arXiv:0905.0636 [astro-ph.HE]].
- [35] M. Cirelli, J. M. Cline, *Phys. Rev.* **D82**, 023503 (2010). [arXiv:1005.1779 [hep-ph]].
- [36] P. Gondolo, J. Edsjo, P. Ullio *et al.*, *JCAP* **0407** (2004), 008. [astro-ph/0406204].
- [37] F. Dick and J. W. Norbury, *Eur. J. Phys.* **30** (2009), 403.
- [38] S. Sivertsson, J. Edsjo, *Phys. Rev.* **D81**, 063502 (2010). [arXiv:0910.0017 [astro-ph.HE]].
- [39] P. Schuster, N. Toro, I. Yavin, *Phys. Rev.* **D81**, 016002 (2010). [arXiv:0910.1602 [hep-ph]].
- [40] Giglietto, N., & Fermi-LAT Collaboration 2010, *MmSAI*, 81, 99
- [41] D. Tucker-Smith and N. Weiner, *Phys. Rev.* **D64** (2001), 043502. [arXiv:hep-ph/0101138].
- [42] D. P. Finkbeiner and N. Weiner, *Phys. Rev.* **D76** (2007), 083519. [arXiv:astro-ph/0702587].
- [43] B. Batell, M. Pospelov, A. Ritz *et al.*, *Phys. Rev.* **D81** (2010) 075004. [arXiv:0910.1567 [hep-ph]].
- [44] I. Cholis, N. Weiner, [arXiv:0911.4954 [astro-ph.HE]].
- [45] S. Nussinov, L. -T. Wang, I. Yavin, *JCAP* **0908** (2009), 037. [arXiv:0905.1333 [hep-ph]].
- [46] A. Menon, R. Morris, A. Pierce *et al.*, *Phys. Rev.* **D82** (2010), 015011. [arXiv:0905.1847 [hep-ph]].
- [47] R. W. Atkins, W. Benbow, D. Berley *et al.*, *Phys. Rev.* **D70**, 083516 (2004).
- [48] The factor $\alpha(E)$ is not exactly equal to 1/100 (that is the exact ratio between the sizes of the real and simulated event samples), because in the randomization process only the overall number of simulated events is fixed, but the simulated events in individual energy bins can change. However, since the size of the simulated data sample is large, $\alpha(E) \simeq 1/100$ in each energy bin.